Journal of Molecular Structure 1353 (2026) 144494

Contents lists available at ScienceDirect

Journal of Molecular Structure

journal homepage: www.elsevier.com/locate/molstr

Synthesis, structural studies, cytotoxicity and computational evaluation of 1,3,4-oxadiazolyl-thio-oxazines as potential NF-κB inhibitors in breast cancer

Bhanuprakash C. Narasimhachar [a], Keshav Kumar Harish [b], Omantheswara Nagaraja [b], Divakar Vishwanath [c], Hediyala B Chandrashekar [d], Mamatha Shinduvalli Kempasiddegowda [e], Mahendra Madegowda [b], Peter E. Lobie [e], Kanchugarakoppal S. Rangappa [c], Basappa Basappa [c,*], Paduvalahippe Gowdegowda Chandrashekara [a,*]

[a] Department of Chemistry, Yuvaraja's College, University of Mysore, Mysuru, Karnataka 570005, India
[b] Department of Studies in Physics, University of Mysore, Manasagangotri, Mysore 570006, India
[c] Laboratory of Chemical Biology, Department of Studies in Organic Chemistry, University of Mysore, Mysore, Karnataka 570006, India
[d] Regional Science Forensic Laboratory, Mysuru, Karnataka 570012, India
[e] Tsinghua Shenzhen International Graduate School (SIGS), Tsinghua University, Shenzhen 518055, China

ARTICLE INFO

Keywords:
1,3,4-oxadiazolyl thio-oxazines
Single-crystal x-ray diffraction
Density functional theory
NF-κB inhibition
Molecular docking
Molecular dynamics simulation

ABSTRACT

In this study, eleven 1,3,4-oxadiazolyl-thio-oxazines (4a–4k) were synthesized and characterized using $^{1}H/^{13}C$ NMR, IR spectroscopy, and mass spectrometry. Single-crystal XRD confirmed that 4c crystallized in the monoclinic *$P2_1/n$ space group*, revealing key intermolecular interactions through Hirshfeld surface analyses. DFT studies using the B3LYP/6–311++*G*(d,p) basis set optimized all the compounds without imaginary frequencies. Frontier molecular orbital analysis provided HOMO–LUMO gaps and global reactivity descriptors, whereas MEP surface analysis offered insights into the charge distribution and potential intermolecular interactions of the optimized structures. For all compounds, the key structural identity of the thiomethylene bond was confirmed by ^{1}H NMR doublets (3.5–4.5 ppm) from diastereotopic coupling near N&S and ^{13}C signals (25–40 ppm) indicating sulfur deshielding. The oxadiazole and oxazine rings were validated by *C=N* (1563–1613 cm^{-1}) and C–O–C (1144–1201 cm^{-1}) absorptions, with IR confirming C–S (696–713 cm^{-1}) and S–CH_2 (~1400 cm^{-1}) linkages. Mass spectra gave $[M + H]^+$ ions as expected, with halogenated derivatives showing predicted isotopic patterns. Furthermore, the theoretical and experimental ^{1}H and ^{13}C NMR data were in agreement, as supported by the correlation coefficient and RMSD values. Alamar Blue assay on MCF-7 breast cancer cells identified 4c (IC_{50} = 33.06 μM) and 4g (IC_{50} = 21.24 μM) as active candidates. It was validated with molecular docking and 100 ns MD simulations, confirming 4*g*'s strong binding affinity towards NF-κB p65 (−8.1 kcal/mol) *via* stable hydrogen bonds and hydrophobic contacts.

1. Introduction

NF-κB is a chief transcription factor involved in biological functions such as immunity, inflammation, survival, and apoptosis [1,2]. Since its discovery as a regulator of immunoglobulin genes *via* DNA binding, NF-κB has become the goal of extensive research [3]. Among the five key proteins, RelA/p65, RelB, c-Rel, NF-κB1/p50, and NF-κB2/p52 the NF-κB family works through blends of these subunits as homodimers or heterodimers to impact the activity of nearly 500 genes [4]. In unstimulated cells, NF-κB is released into the cytoplasm through inhibitor proteins known as IκBs [5]. Stimuli such as TNF-α, infection, or stress activate IKK, which marks IκB for destruction, allowing NF-κB to move

* Corresponding authors at: Department of Chemistry, Yuvaraja's College, University of Mysore, Mysuru 570005 and Laboratory of Chemical Biology, Department of Studies in Organic Chemistry, University of Mysore, Mysore 570006, Karnataka, India.

E-mail addresses: bhanuprakashcn28@gmail.com (B.C. Narasimhachar), keshavkumar@physics.uni-mysore.ac.in (K.K. Harish), omantheswara@physics.uni-mysore.ac.in (O. Nagaraja), divakardivi166@gmail.com (D. Vishwanath), chandrashekarhb77@gmail.com (H.B. Chandrashekar), mamathagowdask@gmail.com (M.S. Kempasiddegowda), mahendra@physics.uni-mysore.ac.in (M. Madegowda), pelobie@sz.tsinghua.edu.cn (P.E. Lobie), rangappaks@gmail.com (K.S. Rangappa), salundibasappa@gmail.com (B. Basappa), pgc2031@gmail.com (P.G. Chandrashekara).

https://doi.org/10.1016/j.molstruc.2025.144494
Received 10 June 2025; Received in revised form 17 October 2025; Accepted 21 October 2025
Available online 22 October 2025

into the nucleus and control gene expression [6]. Dysfunction of NF-κB signalling contributes to inflammation and the growth of various cancers [7]. In breast cancer, NF-κB activation leads to tumor growth, angiogenesis, metastasis, and resistance to therapy [8]. In chronic myelogenous leukemia, constant NF-κB activity helps leukemia cells survive and resist drugs by stalling cell death and boosting growth [9]. The involvement of NF-κB in inflammation and cancer makes it an attractive target for drug development [10].

Multiple therapies target NF-κB signalling; some block upstream activators, such as IKK, preventing NF-κB from binding to DNA [11]. Common drugs such as aspirin, dexamethasone, and TNF-α inhibitors (e.g., infliximab, adalimumab) affect NF-κB activity to different extents [12–15]. Selective NF-κB-targeting small molecules are promising tools for anticancer drug discovery. Oxazine and oxadiazole derivatives (Fig. 1) have shown potential in modifying NF-κB activity. EDPOO suppressed nuclear translocation of NF-κB in LPS-stimulated PC12 cells by 2.95-fold at a concentration of 1 μM. This leads to decreased COX-2, NO, and ROS levels, which are indicative of anti-inflammatory and neuroprotective effects [16]. Similarly, NPO (IC_{50} = 20.3 μM) reduced p65 phosphorylation and DNA binding in HCC cells, diminishing NF-κB-mediation [17]. Pyrimidine-linked oxazine **A** and oxadiazole derivative **B** have demonstrated NF-κB pathway disruption and cytotoxicity in MCF-7 breast cancer and leukemia cells, respectively [18]. CMO, a derivative of 1,3,4-oxadiazole, blocks IκB and p65 activation. Consequently, it inhibits NF-κB and causes cancer cell death and cell cycle arrest [19]. These findings highlight the therapeutic relevance of the oxazine and oxadiazole scaffolds as promising candidates for targeted NF-κB inhibition in cancer therapy. Building on our previously reported work with TRX-01 [20],NPO, and CMO,we designed and synthesized novel 1,3,4-oxadiazolyl-thio-oxazines as hybrid scaffolds that integrate both active pharmacophores for structural diversity.

This study aimed to provide detailed structural insights into newly synthesized 1,3,4-oxadiazolyl-thio-oxazines. We employed single-crystal X-ray diffraction, comprehensive spectroscopic characterization, and density functional theory (DFT) analyses, including Frontier Molecular Orbital (FMO) and Molecular Electrostatic Potential (MEP) studies. Hirshfeld surface investigations were performed to examine the intermolecular interactions in the solid-state. Additionally, cytotoxicity against MCF-7 breast cancer cells and *in silico* studies (ADMET profiling, molecular docking, and molecular dynamics simulations) were employed to establish structure–activity relationships (SAR) and correlate the structural features with the NF-κB inhibitory potential. Overall, this integrated structural and theoretical study primarily contributes new molecular structural information while also highlighting the relevance of these scaffolds in anticancer drug discovery.

2. Methods and materials

2.1. Single crystal X-ray diffraction studies

Single crystals of the synthesized molecule 4c were formed *via* recrystallization in ethyl acetate solvent over a span of 15 days. To

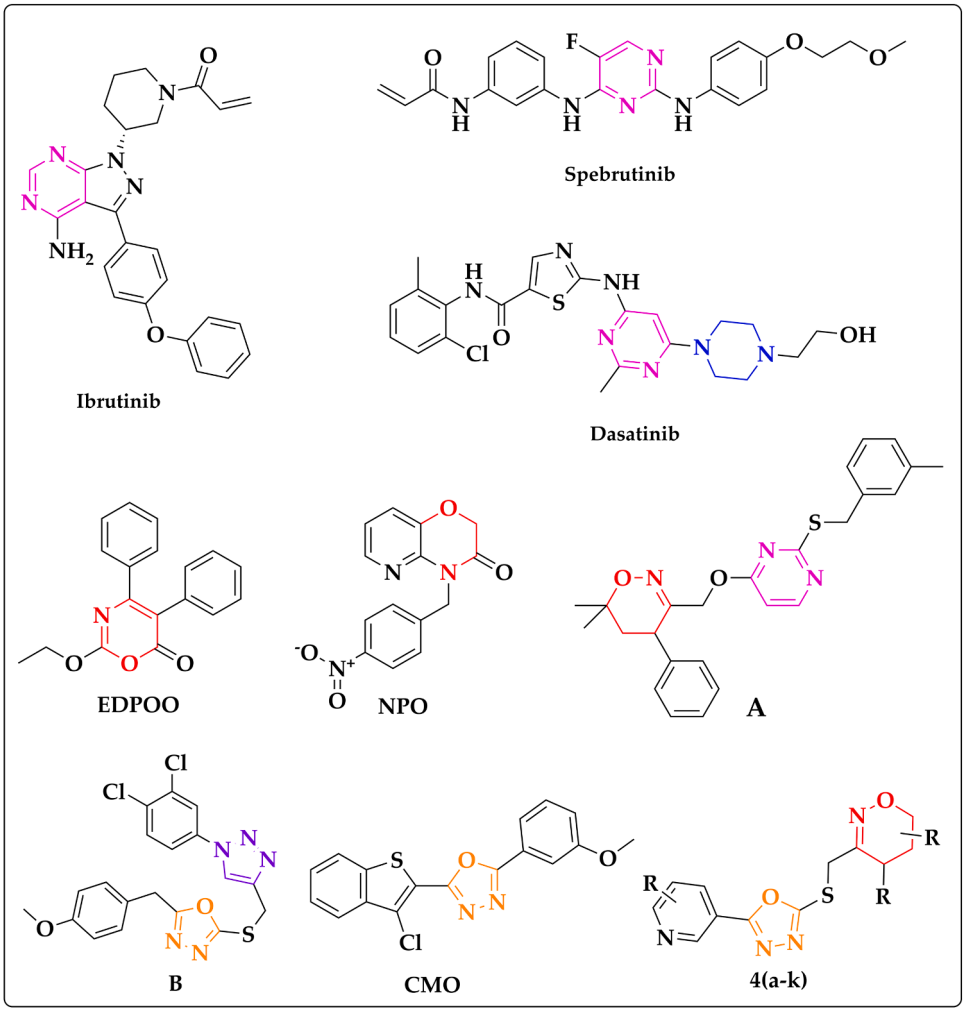

Fig. 1. Reported drugs and potent inhibitors of NF-κB.

perform to diffraction, a well block shaped single crystal of 4c ($C_{20}H_{20}N_4O_2S$, molecular weight: 380.46 g/mol) was chosen. A Bruker D8 Venture diffractometer with a microfocus-sealed X-ray tube and monochromatic mirror optics was used to gather the diffraction data of the crystal. The experiment was carried out at a temperature of 100 K to reduce thermal vibrations and improve data precision. Cu Kα radiation (λ = 1.54178 Å) was used for the diffraction experiments, and the data were acquired in ω and φ scan modes. A resolution of 7.407 pixels mm^{-1} was used as the detector. SADABS 2016/2 was used to apply absorption corrections using the multiscan method [21,22], which greatly enhanced the quality of the intensity data by lowering the wR2 (int) values. The structure was solved using the direct method implemented in SHELXT 2018/2 [23] and refined by the full-matrix least-squares refinement of F^2 using SHELXL 2019/3 [24]. Olex2 1.5, and Mercury [25–27] were used to create molecular visualizations and images, and to create figures that were ready for publication.

2.2. Computational studies

2.2.1. Density functional theory (DFT)

Gaussian09 software was used to perform Density Functional Theory (DFT) experiments [28]. The molecular geometries of all synthesized compounds were modelled and analyzed using GaussView 5, while optimizations of the molecules(4a-4k) were performed at the B3LYP level using the 6–311++*G*(d, p) basis set [29–31]. Further the optimized geometries (Fig. S1) of all eleven synthesized compounds were performed for Potential energy surface (PES) scans using the gas phase system to identify the most stable conformations. The scans were restricted to 10 points with a 1° step size using the same level of basis set. The subsequent structures used to predict IR and NMR spectra of the molecules. All the PES plots and associated data are provided in the Supplementary Information. Root mean square deviation (RMSD) values and the coefficient of determination (R^2) were also obtained to evaluate the correlation between theoretical and experimental data for molecular geometry and NMR spectra.

Theoretical vibrational spectra were generated using DFT calculations at the same functional and basis set with no imaginary frequencies obtained, confirming the stability of the optimized structures, and the simulated peaks showed good correlation with the experimental spectra. Further the experimental and DFT-simulated FTIR spectra were plotted together in a single graph using identical axes scales for direct comparison. Major absorption bands were mentioned in the figure, and the comparative spectra for all synthesized compounds are provided in the Supplementary Information file.

2.3. Experimental

All chemicals and solvents were procured from Sigma-Aldrich (Bangalore, India), unless specified otherwise. The reagents used were picolinic acid (≥98.5 % purity), pyrazine-2-carboxylic acid (≥98.5 % purity), 4-bromobenzoic acid (≥97.5 % purity), hydrazine hydrate (80 % solution in H_2O), potassium carbonate (≥99 % purity), and carbon disulfide (>99 % purity). The solvents employed were absolute ethanol of AR grade and acetone of 99.5 % purity, also AR grade. The concentrated acids used included hydrochloric acid (HCl) at 37 % w/w and sulfuric acid (H_2SO_4) ranging from 95 to 98 % w/w.

The reaction progress was monitored by thin-layer chromatography (TLC) using precoated silica gel 60 F_{254} aluminum-backed plates (Merck, 0.25 mm, 20 × 20 cm), and the plates were visualized under UV light (254 nm). An Agilent mass spectrometer was used to determine the molecular masses of synthesized compounds. Infrared spectra were recorded on a Bruker FTIR spectrometer equipped with a Deuterated Triglycine Sulfate (DTGS) detector. Samples were prepared as KBr pellets, and spectra were collected by averaging 32 scans over the range 4000–400 cm^{-1} with a resolution of 4 cm^{-1}. ^1H and ^{13}C NMR spectra were recorded on Agilent and Jeol spectrophotometers (400 MHz, Santa Clara, CA, USA) using deuterated chloroform ($CDCl_3$, 99.8 atom % D) with tetramethylsilane (TMS) as the internal standard. Chemical shifts are expressed in ppm.

2.4. Synthesis of oxadiazolyl-thio-oxazines

Substituted carboxylic hydrazides (**2**) were synthesized by refluxing acids (1.0 mmol) (**1**) in ethanol with a catalytic amount of concentrated sulfuric acid, followed by the reaction with hydrazine hydrate in ethanol. Subsequently, hydrazide (**2**) was reacted overnight with CS_2 (1.2 mmol) in the presence of NaOH (1.5 mmol) in ethanol. After completion of the reaction, ethanol was reduced under reduced pressure and neutralized by hydrochloric acid, and the solid oxadiazole was filtered off, resulting in compound **(3)**. Finally, compound **(3)** was reacted with substituted oxazine bromides (1.2 mmol) and K_2CO_3 (1.5 mmol) in acetone for 1–2 h. The substituted oxazine bromides were synthesized following the method described by Sukhorukov et al. [32],. After the reaction was complete, acetone was evaporated via vacuum evaporation, and the compounds were isolated by purifying the residue on a silica column using n-hexane and ethyl acetate as eluents **4(a-k)**.

3. Results and discussion

3.1. Crystal structure investigations

Single-crystal X-ray diffraction analysis of 4c (CCDC Deposition No 2386375, http://www.ccdc.cam.ac.uk) was performed using Cu Kα radiation (λ = 1.54178 Å) at 297 K. The compound crystallized in a monoclinic crystal system with the space group $P2_1/n$. The unit cell parameters were determined as follows: a = 5.4759(4) Å, b = 32.440(2) Å, c = 10.2789(7) Å, with a β angle of 95.104(2) ° and a calculated volume of 1818.7(2) $Å^3$. The structure consisted of four formula units per unit cell (Z = 4) with a calculated density of 1.39 Mg m. The final refinement parameters indicated high data quality, with R_1 = 0.034 and

Table 1
Crystal structure data collection and refinement parameters.

Parameters	4c
CCDC deposit No.	2386375
Empirical formula	$C_{20}H_{20}N_4O_2S$
Formula weight	380.46
Temperature (K)	297
Radiation type	CuKα
Wavelength (Å)	1.54178
Crystal system, space group	Monoclinic, $P2_1/n$
Unit cell dimensions	
a, b, c (Å)	5.4759 (4), 32.440 (2), 10.2789 (7)
α β,γ (°)	β= 95.104 (2)
Volume ($Å^3$)	1818.7 (2)
Z	4
Density (calculated) (Mgm^{-3})	1.39
Absorption coefficient (mm^{-1})	1.78
F_{000}	800
Crystal size (mm)	0.17 × 0.15 × 0.11
θ range for data collection	2.7° to 63.9°
Index ranges	−6≤ h ≤ −37≤ k ≤37 −10≤ l ≤11
Reflections collected	31,883
Independent reflections	2992(Rint = 0.067)
Observed [I > 2σ(I)] reflections	2865
Absorption correction	Multi-scan
Refinement method	Full matrix, least-squares on F^2
Data/restraints/parameters	2992 / 0 / 247
Goodness-of-fit on F^2	1.06
Final [I > 2σ (I)]	R1 = 0.034, WR1 = 0.0842
R indices (all data)	R1 = 0.035, WR1 = 0.0849
Largest diff. peak and hole ($e\,Å^{-3}$)	0.24 and −0.20

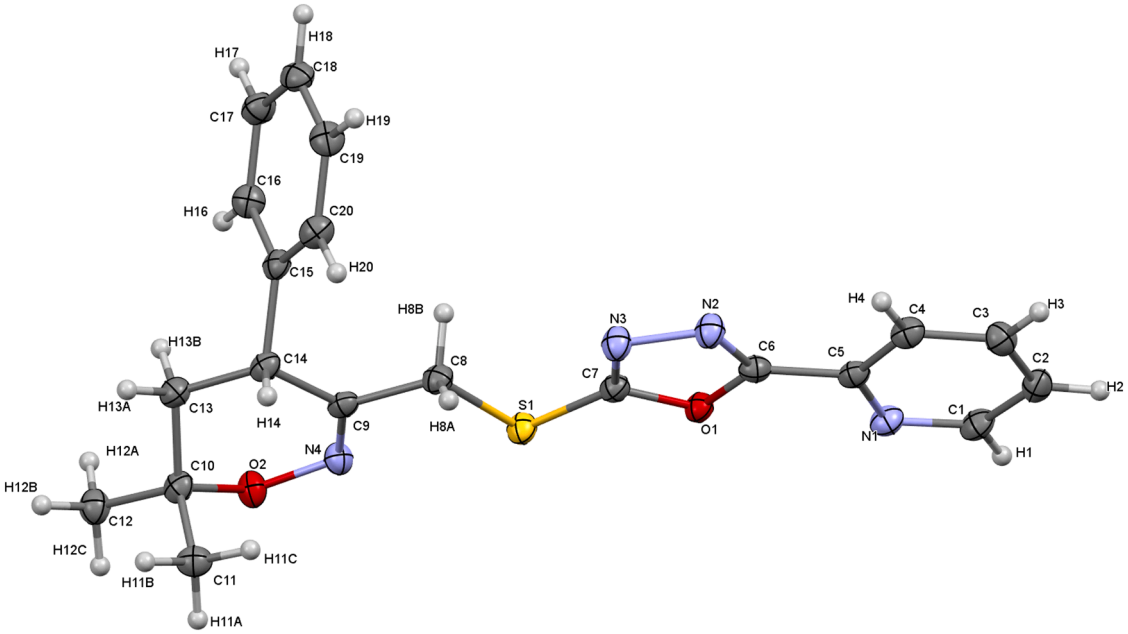

Fig. 2. The Oak ridge thermal ellipsoidal plot (ORTEP) of 4c crystal drawn at 50 % probability.

Table 2
Experimental and theoretical Comparison of Geometrical Bond Lengths (Å) of (4c).

Atoms	XRD (Å)	DFT (Å)	Atoms	XRD (Å)	DFT (Å)
C7–S1	1.735(2)	1.748	C8–S1	1.815(2)	1.841
C6–O1	1.375(2)	1.366	C7–O1	1.365(2)	1.358
N4–O2	1.411(2)	1.379	C10–O2	1.472(2)	1.468
C9–N4	1.282(2)	1.278	N3–N2	1.411(2)	1.393
C6–N2	1.294(2)	1.295	C5–N1	1.344(2)	1.339
C1–N1	1.336(2)	1.334	C7–N3	1.290(2)	1.300
C5–C6	1.462(2)	1.465	C20–C15	1.393(2)	1.398
C14–C15	1.526(2)	1.531	C16–C15	1.395(2)	1.395
C8–C9	1.497(2)	1.508	C14–C9	1.520(2)	1.512
C4–C5	1.392(2)	1.401	H20–C20	0.93	1.084
C19–C20	1.395(2)	1.392	H4–C4	0.93	1.082
C3–C4	1.380(2)	1.388	H2–C2	0.93	1.083
C1–C2	1.386(2)	1.394	RMSD = 0.0891 Å R^2 = 0.98		

wR_2 = 0.0842 for the observed reflections [$I > 2\sigma$ (I)]. The goodness-of-fit for F^2 is 1.06, indicating an appropriate structural refinement model. The absorption coefficient was recorded at 1.78 mm^{-1}, with a multi-scan absorption correction applied. A total of 31,883 reflections were collected, yielding 2992 independent reflections (Rint = 0.067) of which 2865 were considered. Furthermore, the crystal exhibited a well-defined molecular structure with minimal variation in the residual electron density. Complete details of the structural refinement parameters and crystal data are presented in Table 1. At 297 K, the molecular structure maintains a stable conformation without notable atomic displacement or unexpected disorder. The Oak Ridge thermal ellipsoid plot (50 % probability) presented in Fig. 2 confirmed the absence of unusual vibrational behaviour. Additionally, the bond lengths, bond angles, and torsion angles of 4c demonstrated a strong correlation between experimental observations and theoretical predictions, as detailed in Tables 2, 3 and 4. Bond lengths and bond angles displayed close agreement, with RMSD values (0.0891 Å for bond length and 1.759° for bond angles)

Table 3
Experimental and theoretical Comparison of Geometrical Bond Angles (Å) of (4c).

Atoms	XRD	DFT	Atoms	XRD	DFT
C7–S1–C8	94.98(8)	96.39	C6–O1–C7	101.8(1)	102.41
N4–O2–C10	116.9(1)	120.51	O2–N4–C9	118.8(1)	121.40
N3–N2–C6	106.7(1)	106.93	C5–N1–C1	115.9(1)	117.56
N2–N3–C7	105.4(1)	105.78	O1–C6–N2	112.4(1)	112.05
O1–C6–C5	120.8(1)	120.22	N2–C6–C5	126.9(1)	127.71
C20–C15–C14	120.4(1)	123.31	C20–C15–C16	117.9(1)	120.85
C14–C15–C16	121.7(1)	118.44	N4–C9–C8	115.3(1)	116.07
N4–C9–C14	127.5(1)	126.60	C8–C9–C14	117.1(1)	117.09
N1–C5–C6	117.1(1)	117.39	N1–C5–C4	124.3(1)	117.39
C6–C5–C4	118.6(1)	119.21	S1–C7–O1	117.2(1)	116.71
S1–C7–N3	129.1(1)	130.47	C15–C14–C13	113.7(1)	114.98
C9–C14–H14	107.5	105.81	C9–C14–C13	109.5(1)	108.88
H14–C14–C13	107.5	106.54	C20–C19–C18	120.6(2)	120.31
C20–C19–H19	119.7	119.57	C18–C19–H19	119.7	120.11
N1–C1–C2	124.4(1)	123.58	N1–C1–H1	117.8	115.89
C2–C1–H1	117.8	120.52	H11A–C11–H11B	109.5	110.36
O2–C10–C11	109.4(1)	103.31	O2–C10–C13	108.2(1)	109.49
O2–C10–C12	102.7(1)	108.22	C11–C10–C13	113.2(1)	110.65
C11–C10–C12	111.3(1)	110.36	C13–C10–C12	111.5(1)	114.18
C14–C13–C10	111.6(1)	113.35	C14–C13–H13A	109.3	108.20
C14–C13–H13B	109.3	110.42	C10–C13–H13A	109.3	107.82
C10–C13–H13B	109.3	109.54	RMSD = 1.759 Å R^2 = 0.93		

Table 4
Experimental and theoretical Comparison of Geometrical Torsion Angles of (4c).

Atoms	XRD	DFT	Atoms	XRD	DFT
C8-S1-C7-O1	−178.3(1)	178.98	C8-S1-C7-N3	3.5(2)	−1.34
C7-S1-C8-C9	−176.8(1)	−175.80	C7-S1-C8-H8A	−55.9	63.28
C7-S1-C8-H8B	62.4	−52.96	C7-O1-C6-N2	−0.2(2)	0.02
C7-O1-C6-C5	179.0(1)	179.98	C6-O1-C7-S1	−178.3(1)	179.78
C6-O1-C7-N3	0.2(2)	0.06	C10-O2-N4-C9	−22.6(2)	−12.03
N4-O2-C10-C11	−71.8(2)	155.68	N4-O2-C10-C13	51.9(2)	37.75
N4-O2-C10-C12	169.9(1)	−87.29	O2-N4-C9-C8	177.2(1)	−175.71
O2-N4-C9-C14	−0.9(2)	−1.32	C6-N2-N3-C7	0.0(2)	0.11
N3-N2-C6-O1	0.1(2)	−0.085	N3-N2-C6-C5	−179.0(1)	179.95
C1-N1-C5-C6	179.8(1)	−179.99	C1-N1-C5-C4	−0.7(2)	−0.004
C5-N1-C1-C2	0.7(2)	−0.008	C5-N1-C1-H1	−179.3	179.99
N2-N3-C7-S1	178.1(1)	−179.78	N2-N3-C7-O1	−0.1(2)	−0.11
O1-C6-C5-N1	−1.8(2)	−0.59	N4-C9-C14-C13	−7.3(2)	−13.09
C8-C9-C14-C15	48.3(2)	−68.57	C8-C9-C14-H14	−68.9	47.04
C8-C9-C14-C13	174.5(1)	161.23	N1-C5-C4-H4	−179.7	−179.99
N1-C5-C4-C3	0.2(2)	−0.0007	C6-C5-C4-H4	−0.2	−0.0006
C6-C5-C4-C3	179.7(1)	179.98	C15-C20-C19-C18	0.5(3)	−0.08
C15-C20-C19-H19	−179.5	−179.92	H20-C20-C19-C18	−179.5	0.12
H20-C20-C19-H19	0.4	0.120	C5-C4-C3-C2	0.3(2)	0.012
C5-C4-C3-H3	−179.7	−179.99	H4-C4-C3-C2	−179.7	−0.009
C19-C18-C17-H17	−179.1	−179.16	C19-C18-C17-C16	0.9(2)	0.40
C15-C14-C13-C10	161.6(1)	−90.84	C15-C14-C13-H13A	−77.4	32.50
C15-C14-C13-H13B	40.5	149.61	C9-C14-C13-C10	37.0(2)	39.01
C9-C14-C13-H13A	158.1	162.36	C9-C14-C13-H13B	−84	−80.53
H14-C14-C13-C10	−79.5	33.18	H14-C14-C13-H13A	41.5	−83.92
H14-C14-C13-H13B	159.5	33.18	H11A-C11-C10-O2	−57.5	−60.16
H11A-C11-C10-C13	−178.2	177.62	H11A-C11-C10-C12	55.3	52.22
H11B-C11-C10-O2	−177.5	−179.62	H11B-C11-C10-C13	61.8	58.15
H11B-C11-C10-C12	−64.7	−67.23	H11C-C11-C10-O2	62.5	172.36
C11-C10-C12-H12A	−175.2	−177.88	C11-C10-C12-H12B	64.8	61.59
C11-C10-C12-H12C	−55.2	174.67	C13-C10-C12-H12A	57.4	54.73
C13-C10-C12-H12C	177.4	174.67	C13-C10-C12-H12B	−62.6	−65.77
$R^2 = 0.035$ RMSD = 148.279 Å					

within acceptable limits and high R^2 values (0.9782 for bond length and 0.9253 for bond angles), confirming the reliability of the theoretical model. In contrast, torsional angles showed significant deviations between experiment and theory. This discrepancy arises because torsional degrees of freedom are highly sensitive to intermolecular forces and crystal packing effects in the solid state, which are not accounted for in gas-phase DFT calculations. Such deviations are commonly reported and reflect the conformational flexibility of the molecules rather than limitations of the computational approach.

3.2. Crystal structure packing interactions

The crystal packing interactions of 4c along the a-axis are illustrated in Fig. 3, confirms the presence of $Z = 4$ independent molecules within a unit cell. Examination of the hydrogen-bonding interactions in 4c revealed the contribution of the weak C–H···N and C–H···O interactions to the overall packing stability. The molecule results from hydrogen bond interactions, such as C4–H4···N2, exhibiting a donor–acceptor interaction (D···A) at a distance of 3.3828 Å, with an H···A separation of 2.49 Å and a bond angle of 162° Similarly, the C17–H17···O1 interaction

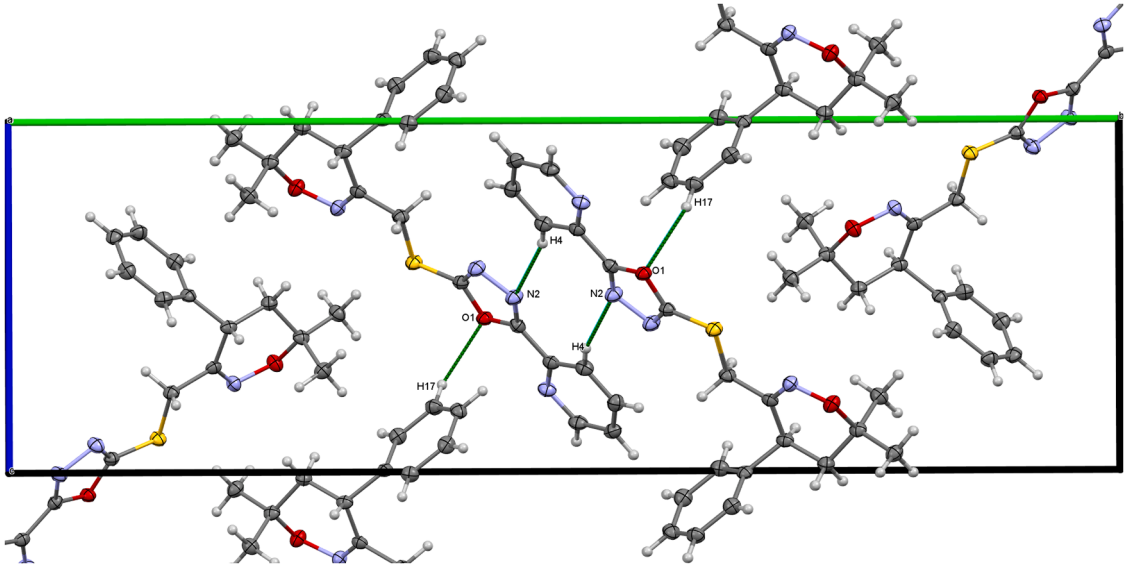

Fig. 3. The crystal packing representation of the 4c representing prominent H-bond interaction (green lines) along a-axis.

Table 5
Prominent hydrogen bond interactions.

Molecule	Interactions	D-H (Å)	H…A (Å)	D…A (Å)	D-H…A (°)
4c	C4-H4…N2[i]	0.93	2.49	3.3828(2)	162
	C17-H17…O1[ii]	0.93	2.59	3.4883(2)	162

i) 1-x,-y,2-z **ii)** x,y,−1 + z.

is noteworthy, with a D···A distance of 3.4883 Å, H···O distance of 2.59 Å, and a bond angle of 162° These interactions are listed in Table 5. Furthermore, the formation of supramolecular synthons through intermolecular hydrogen bonding further reinforces the molecular arrangement within the crystal, as shown in Figs. 3 and S1. The prevalence of such weak non-covalent interactions suggests that the crystal packing is mainly governed by supramolecular forces rather than covalent bonding.

Beyond hydrogen bonding, the structural stability of 4c was further influenced by the X–H···π interactions, as summarized in table S1. The prominent interactions include C4–H2···Cg4 (H···Cg = 2.93 Å, γ = 11.77°, X–H···Cg = 154°), C11–H1A···Cg4 (H···Cg = 2.77 Å, X–H···Cg = 161°), and C17–H17···Cg1 (H···Cg = 2.90 Å, X–H···Cg = 140°). All these interactions involve unique ring systems, such as oxadiazole phenyl rings, which help strengthen the crystal packing through π-electron participation.

In addition, π–π stacking plays a key role in crystal stabilization, as shown in Fig. 4. The most prominent interactions are listed in table S2. The angular parameters (α/β/γ = 2°, 18.9°, and 20.6°) and perpendicular distances (CgI⊥ and CgJ⊥ between 3.3079 and 3.3444 Å) indicated that these rings were nearly parallel, allowing efficient π-electron overlap. Furthermore, the observed slippage distance of 1.144–1.246 Å suggested an offset stacking arrangement, which reduced steric hindrance while maximizing π–π interactions. Combining non-covalent interactions, including hydrogen bonding, X-H···π interactions, and π-π stacking improves 4c's supramolecular organization greatly. Crystallographic investigations revealed a well-ordered monoclinic structure in which weak intermolecular interactions played an important role in defining molecular packing and stability. The observed hydrogen-bonding networks, aromatic stacking, and ring-based interactions provided important information about 4c's structural behaviour. These findings may be useful for developing comparable molecules with higher stabilities and functional characteristics for use in supramolecular chemistry and materials science.

3.3. Hirshfeld surface investigations

Hirshfeld surface analysis is an essential method for investigating the intermolecular interactions in crystalline systems. This technique provides a comprehensive evaluation of different non-covalent interactions by providing a close-up view of the molecular surface and its shape [33–35]. The study utilized parameters such as the shape index and curvedness to characterize weak and strong intermolecular forces within the crystal lattice by mapping the molecular surface according to the electron density distribution, as illustrated in figures S1-S3.

The CrystalExplorer 17.5, software, which generates two-dimensional fingerprint plots considering external (*de*) and internal (*di)* distances relative to the Hirshfeld surface, was used for the analysis. Fig. S2 illustrates this in detail. Strong intermolecular forces are indicated by the red spots on the surface, as identified by the dnorm parameter. The Fig. 5 indicates the red patches represent hydrogen bonds formed when atoms with negative dnorm values join forces. Positive and neutral norm values are represented by blue and white areas on the surface, respectively. It emphasizes hydrogen bonds with nearby molecules by displaying red spots that are concentrated close to oxygen and nitrogen atoms. Two-dimensional fingerprint plots were used to measure the different intermolecular interactions, and the percentage contributions of the structure are shown in Fig. S4. H…H interactions, which are essential for molecular stability, are indicated by the center spike in the plot. The C…H and C… The C interactions that improve the molecular packing are represented by the side wings in the graphs.

It is observed that the compound 4c had the largest percentage of H…H interactions constituted 40.9 % of all connections. As indicated in Fig. S4, the other noteworthy interactions included C—H…H—C (17.9 %), N—H…H—N (17 %), and O—H…H—O (10.2 %). Furthermore, the presence of sulfur atoms in 4c resulted in S-H…H-S interactions, with a 6.9 % contribution. Furthermore NC…C—N (2.1 %), O—H…H—O (1.1 %), S-N….N-S (1 %), N…N (0.5 %), and O—C…C—O (0.2 %) interactions resulted in a lower percentage of contributions. A key metric

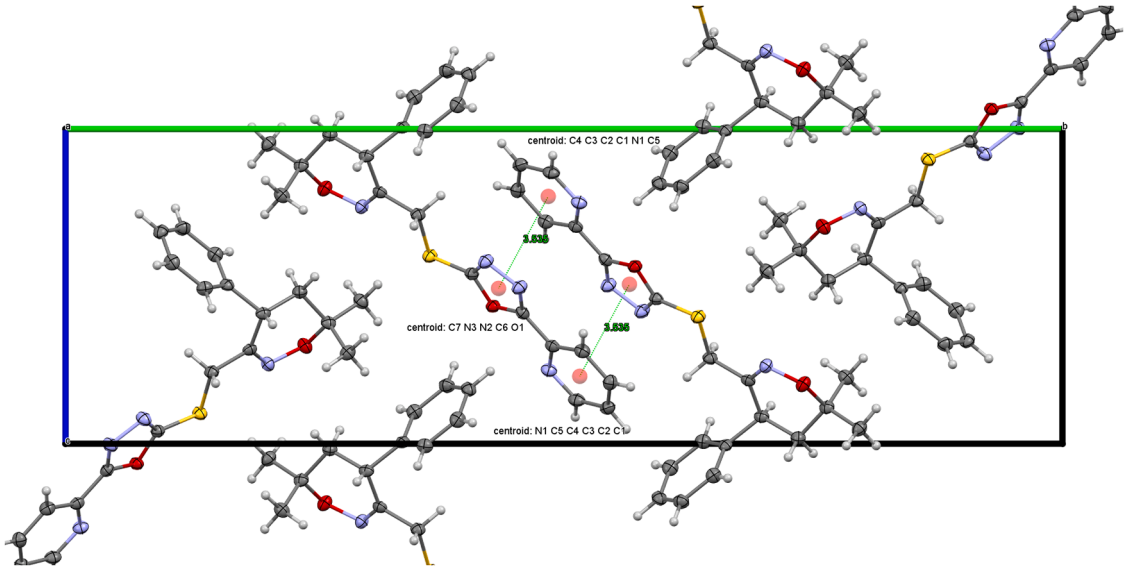

Fig. 4. The unit cell representation of the 4c indicating Cg-Cg interactions (green lines) along a-axis.

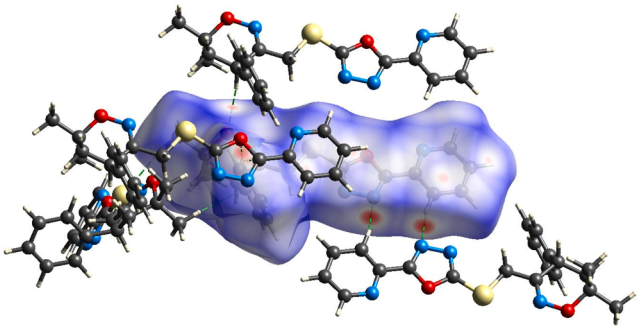

Fig. 5. The Hirshfeld Surface representation mapped on d_{norm} value for 4c indicating the formation of intermolecular interactions.

for assessing the molecular topology, especially in areas with little curvature, is the shape index. It aids in the identification of bulges ($S > 1$) and hollows ($S < 1$), which are denoted by the red and blue triangular regions, respectively [36]. The shape index diagram (Fig. S3(a)) indicates that the triangles highlight the π-π interactions on the molecular surface. These interactions support the stability and packing of the crystal owing to the presence of aromatic phenyl rings in the structure. The curvature of the molecule was determined by its root-mean-square curvature (Fig. S3 (b)). A sharply curved blue line with a high curvature indicates the presence of lone pair-π bonds, whereas flat green regions with a low curvature indicate covalent connections.

3.4. DFT studies

3.4.1. Geometry optimization

All the synthesized derivatives were optimized at the B3LYP/6–311++*G*(d,p) level of theory without any symmetry constraints to obtain their most stable conformations. The optimized geometries correspond to true minima on the potential energy surface, as confirmed by the absence of imaginary frequencies. The calculated structural parameters, including selected bond lengths, bond angles, and dihedral angles (Tables 2, 3 and 4), are in good agreement with experimental single-crystal X-ray diffraction data, confirming the reliability of the theoretical model.The optimized molecular geometries of the derivatives are shown in Fig. S1, which serve as the foundation for further electronic structure analyses such as molecular electrostatic potential map and frontier molecular orbital analyses.

3.4.2. Frontier molecular orbital (FMO) and molecular electrostatic potential (MEP) analysis using density functional theory

To investigate the electronic structural characteristics of the 11 synthesized molecules (4a-4k), Density Functional Theory (DFT) calculations were performed. This analysis focused on Frontier Molecular Orbitals (FMO) and molecular electrostatic potentials (MEP) to evaluate their stability, reactive sites, and interaction potential. The examination included key global chemical descriptors, such as the energies of the highest occupied molecular orbital (HOMO) and lowest unoccupied molecular orbital (LUMO), energy gap (Eg), softness (S), electronegativity (χ), chemical potential (μ), and range of electrostatic potential (ESP), to provide a thorough understanding of the molecular behavior. By assessing the HOMO and LUMO energies of the molecules (Fig. S5), FMO analysis revealed insights into their electronic structures [36]. The highest occupied molecular orbital (HOMO) indicates the ability to donate electrons, whereas the lowest unoccupied molecular orbital (LUMO) indicates the capacity of the molecule to accept electrons. The energy gap (Eg) between these orbitals is a key factor that influences the chemical reactivity [37,38].

The energy gaps (Eg) of the molecular geometries ranged from 3.858 eV for 4d to 5.434 eV for 4j (as Table 6 shows). While 4j suggests that a higher Eg value indicates greater molecular stability and decreased reactivity, the 4d's lower Eg value shows greater reactivity, suggesting that it may be a potential candidate for electron transfer. HOMO orbitals are mainly found on electron-rich atoms of the oxadiazole ring moiety (such as oxygen, nitrogen, and conjugated systems), whereas LUMO orbitals are in electron-deficient areas, marking preferred sites for nucleophilic and electrophilic attacks, respectively. With an electronegativity of 4.943 eV, 4d demonstrates a strong propensity to attract electrons. Other molecules, such as 4b, 4e, and 4g, also exhibit high electronegativity, making them effective electron acceptors. In contrast, molecules 4j and 4k have the lowest electronegativity values (2.675 eV and 2.804 eV, respectively), indicating weaker electron-attracting behavior and reduced reactivity. Softness, which is inversely related to the energy gap, serves as an indicator of molecular reactivity. In line with this, 4d exhibited the highest softness value (0.259 eV−1), confirming its high reactivity, whereas 4j and 4k exhibited the lowest softness values (0.184 eV−1), reinforcing their stability and lower chemical activity.

Additionally, by highlighting regions of electrophilic and nucleophilic contacts, MEP analysis shows (Fig. S6) how charge is distributed inside the molecules. The spectral range of the electrostatic potential was ±4.996e-2 a.u. (4k) to ±7.253e-2 a.u. (4f). A larger ESP range suggests significant variations in the charge density, which influence the interactions between molecules. Compound 4d showed the greatest ESP fluctuation (±7.338e-2 a.u.), suggesting a robust interaction potential with charged or polar entities. The highly negative ESP areas shown in deep red on the MEP plots are sites for nucleophilic attack, mainly located around the oxygen and nitrogen atoms of the oxadiazole ring moiety because of the presence of their lone pairs. The Positive ESP regions in blue represent electrophilic attack sites that are often found near electronegative atoms. In conclusion, FMO and MEP analyses revealed that 4d is among the most reactive molecules owing to its narrow energy gap, high softness, and high electron affinity.

3.5. Chemistry

Picolinic acid, pyrazine-2-carboxylic acid, and 4-bromobenzoic acids were first converted into their corresponding esters (1), which were then

Table 6
Frontier molecular orbital (FMO) chemical reactivity descriptors along with the range of electrostatic potential (ESP) values.

Molecules	Energy E (a.u.)	HOMO E_H (eV)	LUMO E_L(eV)	Energy Gap E_g(eV)	ESP Range (a. u.)	Softness S (eV^{-1})	Chemical Potential μ (eV)	Electro-negativity χ (eV)
4a	−2001.67	−6.427	−1.915	4.512	$\pm5.276e^{-2}$	0.221	4.171	3.844
4b	−1734.34	−6.206	−1.925	4.281	$\pm5.286e^{-2}$	0.233	4.065	3.850
4c	−1542.04	−6.340	−1.632	4.708	$\pm5.418e^{-2}$	0.212	3.986	3.368
4d	−1750.07	−6.298	−2.440	3.858	$\pm6.232e^{-2}$	0.259	4.369	4.943
4e	−1558.07	−6.530	−2.378	4.152	$\pm5.741e^{-2}$	0.240	4.454	4.761
4f	−1694.49	−6.617	−2.057	4.560	$\pm7.253e^{-2}$	0.219	4.337	4.514
4g	−1691.31	−6.421	−1.893	4.528	$\pm6.040e^{-2}$	0.220	4.517	4.488
4h	−2410.16	−6.775	−1.504	5.227	$\pm6.388e^{-2}$	0.191	4.139	3.272
4i	−1911.75	−6.612	−1.635	4.977	$\pm5.892e^{-2}$	0.200	4.123	3.399
4j	−4138.86	−6.530	−1.096	5.434	$\pm5.972e^{-2}$	0.184	3.813	2.675
4k	−4598.49	−6.612	−1.197	5.415	$\pm4.996e^{-2}$	0.184	3.904	2.804

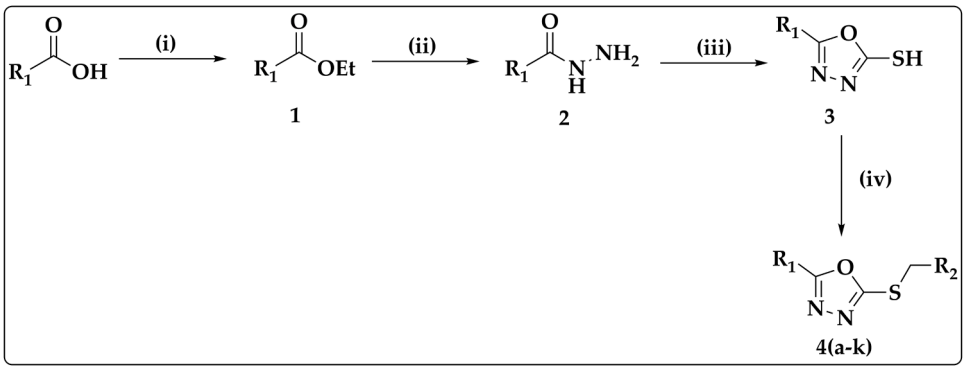

Scheme 1. Synthesis of 1,3,4-oxadiazolyl-thio-oxazines **4(a-i)**. Reaction conditions: (i) picolinic acid, pyrazine-2-carboxylic acid, and 4-bromobenzoic acid, EtOH, H_2SO_4, reflux, 12 h; (ii) $N_2H_4.H_2O$, EtOH, H_2SO_4, reflux, 12 h; (iii) CS_2, KOH, EtOH, reflux, 8 h; (iv) oxazine bromides, K_2CO_3, acetone reflux, 1–2 h.

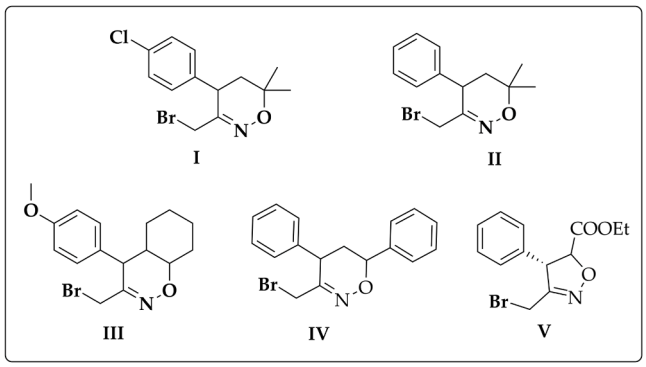

Fig. 6. Structures of substituted oxazines (R_2).

Table 7
List of compounds synthesized.

Products	R_1	R_2	Yield (%)
4a	2-pyridine	I	81
4b	2-pyridine	III	79
4c	2-pyridine	II	86
4d	2-pyrazine	III	81
4e	2-pyrazine	II	76
4f	Pyridine	IV	88
4g	Pyridine	V	81
4h	2-fluoro-3-methyl-5-phenylpyridine	I	80
4i	2-fluoro-3-methyl-5-phenylpyridine	II	85
4j	Bromobenzene	II	81
4k	Bromobenzene	I	80

treated with hydrazine hydrate to obtain the respective hydrazides (2). These hydrazides were subsequently cyclized with carbon disulfide in a basic medium to yield 1,3,4-oxadiazole-2-thiols (3). Finally, the thiols (3) underwent nucleophilic substitution with substituted oxazine bromides (R_2) (Fig. 6) to give 1,3,4-oxadiazolyl-thio-oxazines 4(a–k) (Scheme 1). The plausible mechanism for the synthesis is depicted in Scheme 2 and synthesized compounds are listed in Table 7.

3.6. Spectroscopic characterization

3.6.1. NMR spectra

The ^{1}H NMR spectra of 4a–4k displayed characteristic signals consistent with the proposed structures. A diagnostic feature was the presence of the thiomethylene (–SCH_2–) protons, which observed as doublets in the δ 3.5–4.2 ppm region in all derivatives, confirming the successful incorporation of the oxadiazole–thio–methylene linkage in the synthesized derivatives. The aromatic protons resonated in the δ 7.0–8.9 ppm range, with slight downfield shifts observed in the pyridyl- and pyrazinyl-substituted analogs owing to the deshielding effects of the heteroaromatic rings. For the benzo[e] [1,2]oxazine derivatives (e.g., 4b and 4d), additional multiplets corresponding to aliphatic protons were observed between δ 1.2–2.1 ppm. Compounds bearing geminal dimethyl substituents (e.g., 4a, 4c, 4e, 4 h, and 4k) showed sharp singlets at δ 1.2–1.4 ppm, confirming the substitution at the C-6 position of the oxazine ring.

The ^{13}C NMR spectra further support these assignments. The oxadiazole carbons (*C*=*N* and C–O) consistently resonated in the 150–166 ppm region. The oxazine methylene carbons were identified near δ 40–45 ppm, whereas the oxazine ring carbon adjacent to oxygen observed at approximately δ 75 ppm. Substituted aromatic and heteroaromatic carbons resonated in the δ 120–145 ppm region, consistent with the presence of pyridyl, phenyl, and pyrazinyl groups. The presence of methoxy groups (compounds 4b and 4d) was confirmed by the characteristic signals at δ ~55 ppm.

4-(4-Chlorophenyl)-6,6-dimethyl-3-(((5-(pyridin-2-yl)-1,3,4-oxadiazol-2-yl)thio)methyl)-5,6-dihydro-4H-1,2-oxazine (4a)

^{1}H NMR (400 MHz, $CDCl_3$) δ 8.80 – 8.74 (m, 1H), 8.21 – 8.14 (m, 1H), 7.89 (td, J = 7.8, 1.7 Hz, 1H), 7.51 – 7.43 (m, 1H), 7.34 – 7.29 (m, 2H), 7.20 – 7.12 (m, 2H), 4.02 (d, J = 13.8 Hz, 1H), 3.83 – 3.71 (m, 2H), 2.16 – 2.04 (m, 1H), 1.94 – 1.83 (m, 1H), 1.37 (s, 3H), 1.28 (s, 3H) ; ^{13}C NMR (101 MHz, $CDCl_3$) δ 165.27, 164.52, 153.29, 150.32, 143.06, 137.68, 137.29, 133.61, 129.67, 129.54, 125.91, 122.95, 75.29, 40.57, 37.88, 35.50, 28.25, 22.70.

4-(4-Methoxyphenyl)-3-(((5-(pyridin-2-yl)-1,3,4-oxadiazol-2-yl) thio)methyl)-4a,5,6,7,8,8a-hexahydro-4H-benzo[e] [1,2]oxazine (4b)

^{1}H NMR (400 MHz, $CDCl_3$) δ 8.80 – 8.73 (m, 1H), 8.20 – 8.12 (m, 1H), 7.93 – 7.84 (m, 1H), 7.50 – 7.42 (m, 1H), 7.13 – 7.04 (m, 2H), 6.92 – 6.82 (m, 2H), 4.19 (dd, J = 14.4, 1.8 Hz, 1H), 4.05 (s, 1H), 3.98 (d, J = 14.4 Hz, 1H), 3.77 (s, 3H), 3.37 (s, 1H), 2.11 – 2.04 (m, 1H), 1.76 – 1.55 (m, 4H), 1.47 – 1.25 (m, 4H) ; 13C NMR (101 MHz, $CDCl_3$) δ 165.20, 165.03, 158.87, 151.10, 150.27, 143.17, 137.24, 132.51, 129.19, 125.80, 122.88, 114.44, 69.11, 55.29, 44.76, 38.96, 36.10, 29.07, 27.51, 24.92, 19.91.

6,6-Dimethyl-4-phenyl-3-(((5-(pyridin-2-yl)-1,3,4-oxadiazol-2-yl) thio)methyl)-5,6-dihydro-4H-1,2-oxazine (4c)

^{1}H NMR (400 MHz, $CDCl_3$) δ 8.79 – 8.73 (m, 1H), 8.19 – 8.12 (m, 1H), 7.88 (td, J = 7.8, 1.7 Hz, 1H), 7.50 – 7.42 (m, 1H), 7.33 (t, J = 7.4 Hz, 2H), 7.27 – 7.17 (m, 3H), 4.02 (d, J = 14.5 Hz, 1H), 3.82 – 3.70 (m, 2H), 2.16 – 2.04 (m, 1H), 1.97 – 1.90 (m, 1H), 1.36 (s, 3H), 1.28 (s, 3H); ^{13}C NMR (101 MHz, $CDCl_3$) δ 165.19, 164.72, 153.75, 150.28, 143.15, 139.18, 137.25, 129.35, 128.30, 127.68, 125.86, 122.93, 75.27, 40.63, 38.54, 35.60, 28.29, 22.72

4-(4-Methoxyphenyl)-3-(((5-(pyrazin-2-yl)-1,3,4-oxadiazol-2-yl) thio)methyl)-4a,5,6,7,8,8a-hexahydro-4H-benzo[e] [1,2]oxazine (4d)

^{1}H NMR (400 MHz, $CDCl_3$) δ 9.42 – 9.36 (m, 1H), 8.76 – 8.72 (m, 2H), 7.09 (d, J = 8.8 Hz, 2H), 6.87 (d, J = 8.6 Hz, 2H), 4.21 (d, J = 14.5

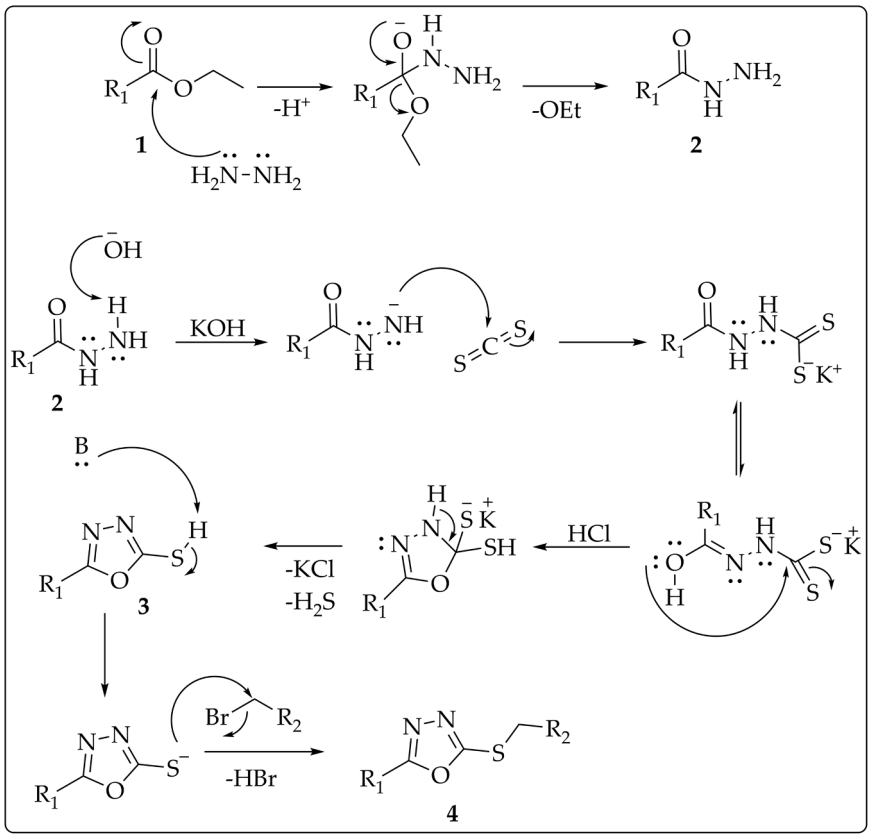

Scheme 2. Plausible mechanism for the synthesis of 1,3,4-oxadiazolyl-thio-oxazines.

Hz, 1H), 4.02 (t, J = 14.6 Hz, 2H), 3.78 (s, 3H), 3.35 (d, J = 1.6 Hz, 1H), 2.06 (s, 1H), 1.71 – 1.23 (m, 8H) ; ^{13}C NMR (101 MHz, $CDCl_3$) δ 166.09, 163.21, 158.90, 150.91, 146.43, 144.59, 143.92, 139.30, 132.44, 129.17, 114.47, 69.17, 55.30, 44.86, 38.97, 36.16, 29.05, 27.53, 24.91, 19.90

6,6-Dimethyl-4-phenyl-3-(((5-(pyrazin-2-yl)-1,3,4-oxadiazol-2-yl) thio)methyl)-5,6-dihydro-4H-1,2-oxazine (4e)

^{1}H NMR (400 MHz, $CDCl_3$) δ 9.39 (d, J = 1.5 Hz, 1H), 8.78 – 8.71 (m, 2H), 7.35 (t, J = 7.4 Hz, 2H), 7.28 – 7.21 (m, 3H), 4.03 (d, J = 14.6 Hz, 1H), 3.82 (d, J = 14.5 Hz, 1H), 3.73 (dd, J = 11.9, 7.8 Hz, 1H), 2.14 (dd, J = 13.7, 7.8 Hz, 1H), 2.01 – 1.90 (m, 1H), 1.37 (s, 3H), 1.29 (s, 3H) ; ^{13}C NMR (101 MHz, $CDCl_3$) δ 165.67, 163.34, 153.48, 146.48, 144.61, 143.95, 139.29, 139.11, 129.39, 128.30, 127.73, 75.34, 40.59, 38.65, 35.60, 28.28, 22.75.

4,6-Diphenyl-3-(((5-(pyridin-2-yl)-1,3,4-oxadiazol-2-yl)thio) methyl)-5,6-dihydro-4H-1,2-oxazine (4f)

^{1}H NMR (400 MHz, $CDCl_3$) δ 8.79 – 8.75 (m, 1H), 8.22 – 8.14 (m, 1H), 7.89 (td, J = 7.8, 1.7 Hz, 1H), 7.47 – 7.24 (m, 12H), 4.93 (ddd, J = 27.9, 11.6, 2.2 Hz, 1H), 4.28 (d, J = 14.5 Hz, 1H), 4.15 – 3.93 (m, 2H), 2.61 – 2.39 (m, 1H), 2.32 – 2.07 (m, 1H), 1.44 – 1.08 (m, 1H) ; ^{13}C NMR (101 MHz, $CDCl_3$) δ 165.12, 165.00, 152.48, 150.29, 143.16, 140.41, 137.28, 129.32, 128.54, 128.32, 128.17, 127.68, 126.62, 125.86, 122.93, 78.39, 38.68, 35.92, 34.16

Ethyl(4S)-4-phenyl-3-(((5-(pyridin-2-yl)-1,3,4-oxadiazol-2-yl)thio) methyl)-4,5-dihydroisoxazole-5-carboxylate (4g)

^{1}H NMR (400 MHz, $CDCl_3$) δ 8.78 (d, J = 4.4 Hz, 1H), 8.18 (dt, J = 7.9, 1.1 Hz, 1H), 7.90 (td, J = 7.8, 1.7 Hz, 1H), 7.54 – 7.45 (m, 1H), 7.38 – 7.29 (m, 3H), 7.24 (d, J = 1.7 Hz, 2H), 4.97 (d, J = 5.3 Hz, 1H), 4.79 (d, J = 5.3 Hz, 1H), 4.34 – 4.21 (m, 3H), 4.04 – 3.90 (m, 1H), 1.30 (t, J = 7.1 Hz, 3H) ; ^{13}C NMR (101 MHz, $CDCl_3$) δ 169.13, 165.22, 163.97, 156.19, 150.27, 142.94, 137.40, 135.99, 129.51, 128.69, 127.72, 127.67, 126.00, 122.96, 86.44, 62.20, 58.80, 27.38, 14.09.

4-(4-Chlorophenyl)-3-(((5-(4-(6-fluoro-5-methylpyridin-3-yl) benzyl)-1,3,4-oxadiazol-2-yl)thio)methyl)-6,6-dimethyl-5,6-dihydro-4H-1,2-oxazine (4h)

^{1}H NMR (400 MHz, $CDCl_3$) δ 8.23 (s, 1H), 7.78 (dd, J = 9.3, 1.6 Hz, 1H), 7.53 (d, J = 8.3 Hz, 2H), 7.39 (d, J = 8.2 Hz, 2H), 7.34 (d, J = 8.4 Hz, 2H), 7.18 – 7.13 (m, 2H), 4.21 (s, 2H), 3.91 (d, J = 14.5 Hz, 1H), 3.73 (dd, J = 11.9, 7.8 Hz, 1H), 3.58 (d, J = 13.5 Hz, 1H), 2.37 (s, 3H), 2.10 (dd, J = 13.7, 7.8 Hz, 1H), 1.91 – 1.84 (m, 1H), 1.35 (s, 3H), 1.20 (s, 3H); ^{13}C NMR (101 MHz, $CDCl_3$) δ 166.83, 163.43, 163.07, 160.70, 153.22, 142.89, 142.74, 140.26, 140.20, 137.71, 136.34, 134.33, 134.28, 133.61, 133.33, 129.72, 129.59, 129.54, 127.59, 119.73, 119.41, 75.23, 40.43, 37.72, 35.44, 31.50, 29.66, 28.26, 22.56, 14.62.

3-(((5-(4-(6-Fluoro-5-methylpyridin-3-yl)benzyl)-1,3,4-oxadiazol-2-yl)thio)methyl)-6,6-dimethyl-4-phenyl-5,6-dihydro-4H-1,2-oxazine (4i)

^{1}H NMR (400 MHz, $CDCl_3$) δ 8.22 (s, 1H), 7.78 (d, J = 6.9 Hz, 1H), 7.52 (d, J = 8.2 Hz, 2H), 7.41 – 7.31 (m, 5H), 7.21 (d, J = 6.8 Hz, 2H), 4.26 – 4.16 (m, 2H), 3.91 (d, J = 14.4 Hz, 1H), 3.72 (dd, J = 11.9, 7.8 Hz, 1H), 3.60 (d, J = 14.9 Hz, 1H), 2.37 (s, 3H), 2.11 (dd, J = 13.6, 7.8 Hz, 1H), 1.91 (d, J = 13.6 Hz, 1H), 1.35 (s, 3H), 1.21 (s, 3H) ; ^{13}C NMR (101 MHz, $CDCl_3$) δ 166.72, 163.58, 163.06, 160.69, 153.77, 142.88, 142.73, 140.26, 140.20, 139.21, 136.31, 134.35, 134.30, 133.39, 132.08, 130.56, 129.60, 129.35, 128.33, 127.70, 127.57, 119.73, 119.40, 75.22, 40.53, 38.31, 35.54, 31.50, 28.30, 22.59, 14.62.

3-(((5-(4-Bromobenzyl)-1,3,4-oxadiazol-2-yl)thio)methyl)-6,6-dimethyl-4-phenyl-5,6-dihydro-4H-1,2-oxazine (4j)

^{1}H NMR (400 MHz, $CDCl_3$) δ 7.49 (d, J = 8.3 Hz, 2H), 7.38 – 7.29 (m, 3H), 7.18 (dd, J = 12.6, 7.6 Hz, 4H), 4.10 (s, 2H), 3.90 (d, J = 14.4 Hz, 1H), 3.71 (dd, J = 11.9, 7.8 Hz, 1H), 3.58 (d, J = 14.4 Hz, 1H), 2.11 (dd, J = 13.7, 7.8 Hz, 1H), 1.98 – 1.87 (m, 1H), 1.36 (s, 3H), 1.19 (s, 3H); ^{13}C NMR (101 MHz, $CDCl_3$) δ 166.38, 163.58, 153.71, 139.22, 132.48, 132.07, 130.54, 129.33, 128.31, 127.68, 121.69, 75.18, 40.55, 38.28, 35.54, 31.28, 28.29, 22.58.

3-(((5-(4-Bromobenzyl)-1,3,4-oxadiazol-2-yl)thio)methyl)-4-(4-chlorophenyl)-6,6-dimethyl-5,6-dihydro-4H-1,2-oxazine (4k)

^{1}H NMR (400 MHz, $CDCl_3$) δ 7.49 (d, $J = 8.4$ Hz, 2H), 7.33 (d, $J = 8.4$ Hz, 2H), 7.16 (t, $J = 8.3$ Hz, 4H), 4.11 (s, 2H), 3.90 (d, $J = 14.4$ Hz, 1H), 3.71 (dd, $J = 11.8$, 7.8 Hz, 1H), 3.56 (d, $J = 13.5$ Hz, 1H), 2.09 (dd, $J = 13.7$, 7.8 Hz, 1H), 1.87 (dd, $J = 13.6$, 11.9 Hz, 1H), 1.36 (s, 3H), 1.18 (s, 3H) ; ^{13}C NMR (101 MHz, $CDCl_3$) δ 166.22, 163.42, 153.55, 139.06, 132.31, 131.91, 130.37, 129.16, 128.14, 127.51, 121.52, 75.02, 40.38, 38.12, 35.37, 31.12, 28.12, 22.42.

3.6.2. Comparative analysis of theoretical and experimental NMR spectra

A comparison of the experimental and theoretical chemical shifts revealed consistently high correlation coefficients ($R^2 > 0.98$) (Supplementary, Page: S45 – S88) for both the ^{1}H and ^{13}C NMR spectra for all compounds (4a–4k), along with low RMSD values use same level of basis set, demonstrating the reliability of the computational method. A tabulation of the RMSD values for each compound is included in the tables S8 and S9.

3.6.3. FTIR spectra

The FTIR spectra of the synthesized compounds (4a–4k) exhibited characteristic absorption bands that confirmed the presence of key functional groups. A strong *C=N* stretching vibration of the 1,3,4-oxadiazole ring was consistently observed in the 1563–1613 cm^{-1} region. IR bands observed in the 1144–1201 cm^{-1} region can be assigned to C-O-C stretching modes of the oxazine ring or methoxy substituents which are expected in that range, further confirming the heterocyclic framework. Distinct C–S stretching bands were recorded in the 696–713 cm^{-1} region, while a weak S–CH_2 bending vibration near 1400 cm^{-1} supported the presence of the thioether linkage.

Compound-specific features were also observed. For compound 4g, an additional strong band at 1732 cm^{-1} was attributed to the ester $C = O$ stretching. Similarly, methoxy-substituted derivatives (4a and 4b) displayed characteristic absorptions associated with the aryl methyl ether functionality. Compounds with halogen substituents (4a, 4h, 4k) exhibited additional vibrations in the fingerprint region (600–800 cm^{-1}), confirming the presence of C–Cl or C–Br bonds. Collectively, the FTIR data strongly supported the structural assignments of all synthesized derivatives by confirming the presence of oxadiazole, oxazine, and thioether functionalities, along with substituent-specific signatures.

3.6.4. Comparative analysis of theoretical and experimental FTIR spectra

The experimental FTIR spectra of compounds 4a–4k were in good agreement with the theoretically simulated spectra obtained from DFT calculations (Fig. S7). The characteristic stretching vibrations, particularly those corresponding to *C=N*, C–O–C, and C–S functionalities, were reproduced well in the theoretical profiles, validating the structural assignments. Minor deviations in absorption frequencies were attributed to solvent effects and basis set limitations.

3.6.5. Mass spectral studies

The LCMS analysis of compounds (4a–4k) showed molecular ion peaks $[M + H]^+$ in close agreement with their calculated values, confirming their molecular masses. Compounds bearing halogen substituents further exhibited the characteristic isotopic patterns, consistent with the presence of Cl and Br atoms (Supplementary, Page: S23-S44).

3.7. Biology

Comprehensive biological studies, including cytotoxicity evaluation, ADME profiling, computational analyses, and structure–activity relationship (SAR) studies, are provided in the Supporting Information (Page: S13-S22).

4. Conclusion

In this study, eleven 1,3,4-oxadiazolyl-thio-oxazine derivatives (4a–4k) were synthesized and structurally characterized using ^{1}H/^{13}C NMR, IR spectroscopy, and mass spectrometry. Single-crystal XRD confirmed that compound 4c crystallized in the monoclinic $P2_1/n$ space group with reliable refinement values. The structure displayed hydrogen bonding, aromatic stacking, and van der Waals interactions, while the Hirshfeld analysis indicated that 40.9 % of the H···H contacts were the dominant stabilizing forces. The HOMO orbitals were localized on the oxadiazole moiety, whereas the LUMOs were found in electron-deficient regions. Among the studied derivatives, compound 4d was identified as the most reactive molecule, as revealed by FMO and MEP analyses, owing to its narrow energy gap, high softness, and greater electron affinity. MEP surface mapping identified nucleophilic sites near the oxygen and nitrogen atoms. The simulated NMR and FTIR spectra agreed well with the experimental results, with high correlations and low RMSDs, confirming the model reliability. Alamar Blue assay on MCF-7 breast cancer cell line (Supplementary, Page: S13-S22) showed 4c and 4g were moderately cytotoxic to MCF-7 cells ($IC_{50} = 33.06$ μM and 21.24 μM). Molecular docking and 100 ns MD simulations with NF-κB p65 (PDB ID: 1IKN) demonstrated that 4g exhibited stronger binding affinity (−8.1 kcal/mol) and superior stability compared to 4c, supported by persistent hydrogen bonds and hydrophobic contacts. Overall, this study presents a comprehensive structural and theoretical characterization of 1,3,4-oxadiazolyl-thio-oxazines, supported by crystallography, spectroscopy, DFT, with docking and dynamics providing preliminary insights into their biological potential.

Supporting information

The supporting information includes spectral data, Biology results, and DFT studies with comparisons between theoretical and experimental data for compounds 4(a–k).

Funding

Bhanuprakash C Narasimhachar thanks Other Backwards Clause Cell, University of Mysore, Karnataka, for the fellowship during this study.

Author declaration

We used ChatGPT (OpenAI, 2024) to improve the readability and language of the manuscript. The authors reviewed and verified the content to ensure accuracy and integrity.

Ethical approval

Not applicable.

Consent to participate

Not applicable.

CRediT authorship contribution statement

Bhanuprakash C. Narasimhachar: Writing – review & editing, Writing – original draft, Visualization, Validation, Software, Methodology, Investigation, Formal analysis, Data curation, Conceptualization. **Keshav Kumar Harish:** Software, Formal analysis, Data curation, Conceptualization. **Omantheswara Nagaraja:** Visualization, Software, Formal analysis, Data curation, Conceptualization. **Divakar Vishwanath:** Methodology, Conceptualization. **Hediyala B Chandrashekar:** Formal analysis, Data curation. **Mamatha Shinduvalli Kempasiddegowda:** Formal analysis, Data curation. **Mahendra Madegowda:** Methodology, Investigation. **Peter E. Lobie:** Validation, Data curation. **Kanchugarakoppal S. Rangappa:** Project administration. **Basappa Basappa:** Supervision, Conceptualization. **Paduvalahippe Gowdegowda Chandrashekara:** Supervision, Conceptualization.

Declaration of competing interest

The authors report there are no competing interests to declare.

Acknowledgements

The authors gratefully acknowledge the Indian Institute of Chemical Biology, Kolkata, India for providing access to the single-crystal X-ray diffraction facility and valuable assistance with data collection and structure refinement.

Supplementary materials

Supplementary material associated with this article can be found, in the online version, at doi:10.1016/j.molstruc.2025.144494.

Data availability

The datasets in this study are available from the corresponding author upon reasonable request.

References

[1] A.R. Liu, P. Ramakrishnan, Regulation of nuclear factor-kappaB function by O-GlcNAcylation in inflammation and cancer, Front. Cell Dev. Biol. 9 (2021), https://doi.org/10.3389/fcell.2021.751761.
[2] Y. Li, B. Zhao, J. Peng, H. Tang, S. Wang, S. Peng, F. Ye, J. Wang, K. Ouyang, J. Li, M. Cai, Y. Chen, Inhibition of NF-κb signaling unveils novel strategies to overcome drug resistance in cancers, Drug Resist. Updat. 73 (2024) 101042, https://doi.org/10.1016/j.drup.2023.101042.
[3] H. Jo, M.-H. Choi, A.S. Kumar, Y. Jung, S.E. Kim, J. Yun, J.S. Kang, Y. Kim, S. Han, J. Jung, J. Cho, K. Lee, J. Kwak, H. Lee, Development of novel 1,2,3,4-tetrahydroquinoline scaffolds as potent NF-κb inhibitors and cytotoxic agents, ACS Med. Chem. Lett. 7 (2016) 385–390, https://doi.org/10.1021/acsmedchemlett.6b00004.
[4] E. Jimi, T. Katagiri, Critical roles of NF-κb signaling molecules in bone metabolism revealed by genetic mutations in osteopetrosis, Int. J. Mol. Sci. 23 (2022) 7995, https://doi.org/10.3390/ijms23147995.
[5] S. Yamauchi, H. Ito, A. Miyajima, IκBη, a nuclear iκb protein, positively regulates the NF-κb–mediated expression of proinflammatory cytokines, Proc. Natl. Acad. Sci. 107 (2010) 11924–11929, https://doi.org/10.1073/pnas.0913179107.
[6] W. Wu, L. Li, X. Su, Z. Zhu, X. Lin, J. Zhang, Z. Zhuang, H. Cai, W. Huang, Nuclear factor-kappaB regulates the transcription of NADPH oxidase 1 in Human alveolar epithelial cells, (2020). https://doi.org/10.21203/rs.3.rs-132252/v1.
[7] T. Zhang, C. Ma, Z. Zhang, H. Zhang, H. Hu, NF-κb signaling in inflammation and cancer, MedComm. (2020) 2 (2021) 618–653, https://doi.org/10.1002/mco2.104.
[8] L. Zhu, Y. Zhang, B. Wang, Y. Li, Y.-Q. Zheng, L. Sun, L. Tian, T. Chen, J. Wang, PCDHB17P/miR-145-3p/MELK/NF-κb feedback loop promotes metastasis and angiogenesis of breast cancer, front, Oncol. 11 (2021), https://doi.org/10.3389/fonc.2021.660307.
[9] B. Basappa, Y.Y. Jung, A. Ravish, X. Zhang, A. Swamynayaka, M. Mahendra, V. Pandey, P.E. Lobie, G. Sethi, K.S. Ahn, Methyl-thiol-bridged oxadiazole and triazole heterocycles as inhibitors of NF-κb in chronic myelogenous leukemia cells, Biomedicines 11 (2023) 1662, https://doi.org/10.3390/biomedicines11061662.
[10] J. Shin, J. Lim, D. Han, S. Lee, N.S. Sung, J.-S. Kim, D.K. Kim, H.Y. Lee, S.K. Lee, J. Shin, J.S. Kim, H. Park, TBK1 Inhibitor Amlexanox exerts anti-cancer effects against endometrial cancer by regulating AKT/NF-κb signaling, Int. J. Biol. Sci. 21 (2025) 143–159, https://doi.org/10.7150/ijbs.100212.
[11] S. Shahabi, M.R. Maurya, S. Subramaniam, G. Ghosh, Tumor suppressor NME1/NM23-H1 modulates DNA binding of NF-κb RelA, (2024). https://doi.org/10.21203/rs.3.rs-5242004/v1.
[12] F. Din, L.A. Stark, M.G. Dunlop, Aspirin-induced nuclear translocation of nfκb and apoptosis in colorectal cancer is independent of P53 status and DNA mismatch repair proficiency, Br. J. Cancer 92 (2005) 1137–1143, https://doi.org/10.1038/sj.bjc.6602455.
[13] H. Yu, L. Lin, Z. Zhang, H. Zhang, H. Hu, Targeting NF-κb pathway for the therapy of diseases: mechanism and clinical study, Signal. Transduct. Target. Ther. 5 (2020) 209, https://doi.org/10.1038/s41392-020-00312-6.
[14] S. Dadsetan, T. Balzano, J. Forteza, A. Cabrera-Pastor, L. Taoro-González, V. Hernández-Rabaza, S. Gil-Perotín, L. Cubas-Núñez, J.M. García-Verdugo, A. Agustí, M. Llansola, V. Felipo, Reducing peripheral inflammation with Infliximab reduces neuroinflammation and improves cognition in rats with hepatic encephalopathy, Front. Mol. Neurosci. 9 (2016), https://doi.org/10.3389/fnmol.2016.00106.
[15] J. Xu, S. Guo, R. Xue, L. Xiao, J. Kou, Y. Liu, J. Han, J. Fu, N. Wei, Adalimumab ameliorates memory impairments and neuroinflammation in chronic cerebral hypoperfusion rats, Aging (Albany. NY) 13 (2021) 14001–14014, https://doi.org/10.18632/aging.203009.
[16] N. Ansari, F. Khodagholi, M. Amini, F. Shaerzadeh, Attenuation of LPS-induced apoptosis in NGF-differentiated PC12 cells via NF-κb pathway and regulation of cellular redox status by an oxazine derivative, Biochimie 93 (2011) 899–908, https://doi.org/10.1016/j.biochi.2011.01.012.
[17] C.D. Mohan, H. Bharathkumar, S.Rangappa Dukanya, M.K. Shanmugam, A. Chinnathambi, S.A. Alharbi, T.A. Alahmadi, A. Bhattacharjee, P.E. Lobie, N-substituted pyrido-1, 4-oxazin-3-ones induce apoptosis of hepatocellular carcinoma cells by targeting NF-κb signaling pathway, Front. Pharmacol. 9 (2018) 1125, https://doi.org/10.3389/fphar.2018.01125.
[18] A. Ravish, B.C. Narasimhachar, Z. Xi, D. Vishwanath, A. Mohan, S.L. Gaonkar, P. G. Chandrashekara, K.S. Ahn, V. Pandey, P.E. Lobie, B. Basappa, Development of piperazine- and oxazine-linked pyrimidines as p65 subunit binders of NF–κB in Human breast cancer cells, Biomedicines 11 (2023), https://doi.org/10.3390/biomedicines11102716.
[19] C.D. Mohan, N.C. Anilkumar, S. Rangappa, M.K. Shanmugam, S. Mishra, A. Chinnathambi, S.A. Alharbi, A. Bhattacharjee, G. Sethi, A.P. Kumar, B. Basappa, K.S. Rangappa, Novel 1,3,4-oxadiazole induces anticancer activity by targeting NF-κb in hepatocellular carcinoma cells, Front. Oncol. 8 (2018), https://doi.org/10.3389/fonc.2018.00042.
[20] J. Yuan, B.C. Narasimhachar, A. Ravish, Y. Li, H. Zhang, Q. Wang, Z. Li, J. Huang, B. Wang, G. Wang, K.K. Harish, A. Chinnathambi, C. Govindasamy, M. Mahendra, B. Basappa, Discovery of oxazine-linked pyrimidine as an inhibitor of breast cancer growth and metastasis by abrogating NF-κb activation, Front. Oncol. 14 (2024), https://doi.org/10.3389/fonc.2024.1390992.
[21] L. Krause, R. Herbst-Irmer, G.M. Sheldrick, D. Stalke, Comparison of silver and molybdenum microfocus X-ray sources for single-crystal structure determination, Appl. Crystallogr. 48 (2015) 3–10, https://doi.org/10.1107/S1600576714022985.
[22] B. A, Version, 1 Data Collection and Processing Software, Bruker Analytical X-Ray Instruments, Inc, Madison WI USA, 2009.
[23] G.M. Sheldrick, Crystal structure refinement with SHELXL, Cryst. Struct. Commun. 71 (2015) 3–8, https://doi.org/10.1107/S2053229614024218.
[24] G.M. Sheldrick, SHELXT–Integrated space-group and crystal-structure determination, Found. Crystallogr. 71 (2015) 3–8, https://doi.org/10.1107/S2053273314026370.
[25] L.J. Bourhis, O.V. Dolomanov, R.J. Gildea, J.A. Howard, H. Puschmann, The anatomy of a comprehensive constrained, restrained refinement program for the modern computing environment–Olex2 dissected, Found. Crystallogr. 71 (2015) 59–75, https://doi.org/10.1107/S2053273314022207.
[26] O.V. Dolomanov, L.J. Bourhis, R.J. Gildea, J.A. Howard, H. Puschmann, OLEX2: a complete structure solution, refinement and analysis program, Appl. Crystallogr. 42 (2009) 339–341, https://doi.org/10.1107/S0021889808042726.
[27] C.F. Macrae, I. Sovago, S.J. Cottrell, P.T. Galek, P. McCabe, E. Pidcock, M. Platings, G.P. Shields, J.S. Stevens, M. Towler, Mercury 4.0: from visualization to analysis, design and prediction, Appl. Crystallogr. 53 (2020) 226–235, https://doi.org/10.1107/S1600576719014092.
[28] M. Frisch, gaussian 09, revision d. 01, Gaussian, Inc Wallingford CT 201 (2009).
[29] R. Dennington, T. Keith, J. Millam, GaussView; Semichem Inc, Shawnee Mission KS (2009).
[30] A.D. Becke, Density-functional thermochemistry. III. The role of exact exchange, J. Chem. Phys. 98 (1993) 5648–5652, https://doi.org/10.1063/1.464913.
[31] H.S. Lee, S. Jo, H.-S. Lim, W. Im, Application of binding free energy calculations to prediction of binding modes and affinities of MDM2 and MDMX inhibitors, J. Chem. Inf. Model. 52 (2012) 1821–1832, https://doi.org/10.1021/ci3000997.
[32] A.Y. Sukhorukov, M.A. Kapatsyna, T.L.T. Yi, H.R. Park, Y.A. Naumovich, P. A. Zhmurov, Y.A. Khomutova, S.L. Ioffe, V.A. Tartakovsky, A general metal-assisted synthesis of α-halo oxime ethers from nitronates and nitro compounds, Eur. J. Org. Chem. 2014 (2014) 8148–8159, https://doi.org/10.1002/ejoc.201403083.
[33] P.R. Spackman, M.J. Turner, J.J. McKinnon, S.K. Wolff, D.J. Grimwood, D. Jayatilaka, M.A. Spackman, CrystalExplorer: a program for Hirshfeld surface analysis, visualization and quantitative analysis of molecular crystals, Appl. Crystallogr. 54 (2021) 1006–1011, https://doi.org/10.1107/S1600576721002910.
[34] S.R. Prabhu, V. Upadhyaya, A. Jayarama, Synthesis, crystal structure and Hirshfeld surface analysis of a novel chalcone derivative:(2E)-3-(2, 3-dimethoxyphenyl)-1-(3-nitrophenyl) prop-2-en-1-one, Chem. Data Collect. 11 (2017) 199–210, https://doi.org/10.1016/j.cdc.2017.10.001.
[35] D.A. Zainuri, I.A. Razak, S. Arshad, Molecular structure, DFT studies and Hirshfeld analysis of anthracenyl chalcone derivatives, Struct. Rep. 74 (2018) 780–785, https://doi.org/10.1107/S2056989018006527.
[36] V. Arjunan, A.S.R. Isaac, T. Rani, C. Mythili, S. Mohan, Density functional theory studies on vibrational and electronic spectra of 2-chloro-6-methoxypyridine, in: V. Arjunan, A.S.R. Isaac, T. Rani, C. Mythili, S. Mohan (Eds.), Density functional theory studies on vibrational and electronic spectra of 2-chloro-6-methoxypyridine, Spectrochim. Acta a Mol. Biomol. Spectrosc. 78 (2011) 1625–1632. Density functional theory studies on vibrational and electronicspectra of 2-chloro-6-methoxypyridine, Spectrochim. Acta. A. Mol. Biomol.Spectrosc. 78 (2011) 1625–1632.
[37] R.G. Parr, R.G. Pearson, Absolute hardness: companion parameter to absolute electronegativity, J. Am. Chem. Soc. 105 (1983) 7512–7516, https://doi.org/10.1021/ja00364a005.
[38] B. Kosar, C. Albayrak, Spectroscopic investigations and quantum chemical computational study of (E)-4-methoxy-2-[(p-tolylimino) methyl] phenol, Spectrochim. Acta A Mol. Biomol. Spectrosc. 78 (2011) 160–167, https://doi.org/10.1016/j.saa.2010.09.016.